



HAL
open science

Modeling plasticity of an aluminum 2024T351 thick rolled plate for cold forming applications

Raphaël Cusset, Farida Azzouz, Jacques Besson, Marta Dragon-Louiset,
Vincent Jacques, Henry Proudhon

► To cite this version:

Raphaël Cusset, Farida Azzouz, Jacques Besson, Marta Dragon-Louiset, Vincent Jacques, et al.. Modeling plasticity of an aluminum 2024T351 thick rolled plate for cold forming applications. International Journal of Solids and Structures, 2020, 202, pp.463-474. 10.1016/j.ijsolstr.2020.05.005 . hal-03027179

HAL Id: hal-03027179

<https://hal.science/hal-03027179>

Submitted on 27 Nov 2020

HAL is a multi-disciplinary open access archive for the deposit and dissemination of scientific research documents, whether they are published or not. The documents may come from teaching and research institutions in France or abroad, or from public or private research centers.

L'archive ouverte pluridisciplinaire **HAL**, est destinée au dépôt et à la diffusion de documents scientifiques de niveau recherche, publiés ou non, émanant des établissements d'enseignement et de recherche français ou étrangers, des laboratoires publics ou privés.

Modeling plasticity of an aluminum 2024T351 thick rolled plate for cold forming applications

Raphaël Cusset^a, Farida Azzouz^a, Jacques Besson^a, Marta Dragon-Louiset^b,
Vincent Jacques^b, Henry Proudhon^{a,*}

^a*MINES ParisTech, PSL University, MAT – Centre des matériaux, CNRS UMR 7633,
BP 87 91003 Evry, France*

^b*Dassault Aviation, 78 Quai Marcel Dassault, 92210 Saint-Cloud, France*

Abstract

Sheet metals exhibit plastic anisotropy due to the rolling process. This article focuses on the particular case of an 2024T351 Aluminium alloy thick sheet which showed in addition to the anisotropy of mechanical properties an important evolution of these properties along the thickness. A large series of tension tests performed is carried out using samples machined varying the position along the thickness and the orientation in the rolling plane. Strong variation in terms of elastic limit and ultimate tensile stress are observed. The heterogeneity of the microstructure is studied by EBSD along the plate thickness and correlated with the mechanical properties variations; 4 main zones are identified. The constitutive behaviour of the material is modelled using an anisotropic yield criterion combined to a non-linear hardening rule and one set of parameters is identified for each material layer. The predictive capabilities of the model are illustrated by simulations of notched tension tests with three notch radii. Finally a large structure panel bending test representative of cold forming industrial operations is simulated using the identified model parameters. A very good agreement between the FE results and the experimental strain gauge signals from a scale 1 experiment is observed. This shows the thickness-based identification accurately accounts for the property gradient for large structure panel simulations.

Keywords: Aluminum alloys, Plasticity, Anisotropy, Heterogeneity, thick rolled plate, Metal forming, Structural part

*Corresponding author

Email address: henry.proudhon@mines-paristech.fr (Henry Proudhon)

1. Introduction

Metal forming is one of the most common processes used to give the final shape to mechanical structures [1, 2]. It involves plastic deformation and therefore will modify locally the material properties by work hardening. It is thus critical to be able to simulate accurately the forming operation which in turn requires to model appropriately the constitutive behaviour of the material. As received material for structural parts often comes in plates which are known to have anisotropic plastic properties generated by rolling process. This justify the numerous past studies to model plasticity of metallic sheets and plates [3–5].

In this work, the case of a thick plate made of Al2024T351, a widely used aluminum alloy will be investigated. It is known to be an appropriate material for most forming applications (bending, extruding, stretching) with a good compromise between strength, formability and density [6].

One commonly used strategy to model plasticity consists in defining an equivalent stress $\bar{\sigma}$, depending of material conditions and properties, associated with a yield function $f(\bar{\sigma})$. In the last decades, many models have used only isotropic yield criterion starting by Mises [7] equation based on the shear energy. Other models followed like Hershey [8] then Hosford [9]. Hill first proposed a description of the anisotropy of metal sheets using 6 anisotropic parameters h_i [10]. Karafillis and Boyce [5] provided a major modification with the definition of a special deviator by the linear transformation $\underline{\mathfrak{s}} = \underline{\mathfrak{L}} : \underline{\sigma}$ where the fourth order tensor $\underline{\mathfrak{L}}$ contains the anisotropy parameters. This approach generalized Barlat [4], Tresca and Mises formulation in one expression of $\bar{\sigma}$. Later Bron and Besson improved the expression of $\bar{\sigma}$ with a criteria using 14 parameters [3].

In contrast with all this work, the evolution of the material properties along the thickness of the rolled sheets has not received so much attention. This is especially important for thick plates, where the rolling conditions may induce a particularly non homogeneous strain field. Thick plates are used in many industrial structures where welding or assembling is considered as not desirable. Some authors have studied anisotropy in the specific case of thick plates machining [11–18] and all highlighted the heterogeneity of the microstructure and a gradient of mechanical properties in the plate thickness. In contrary to the classical model identification approach where the material

36 considered as homogeneous, an experimental/modeling strategy needs to be
37 devised.

38 The present work deals with the cold-bending of a 2024T351 structure.
39 The structure of reference, in the form of stiffened panels, was machined
40 from a 60 mm thick rolled plate. During the manufacturing process, such
41 components are cold-bent inducing high strains and residual stresses in lo-
42 calized regions of the structures. In order to predict accurately this residual
43 stress state, an elasto-plastic material model of this thick sheet is required to
44 capture both the anisotropy and the through-thickness property gradient.

45 The paper is organized as follows: section 2 presents the experimental
46 methods to characterize the material and to conduct all the mechanical test-
47 ing, including a scale 1 bending test on a structural panel. Results on the
48 microstructure characterization and elasto-plastic properties are gathered in
49 sections 3 and 4 respectively. Section 5 contains the constitutive modelling,
50 identification and validation on notched-tensile specimens. This is finally
51 followed by the simulation of the cold forming of a panel structure which is
52 compared to the scale 1 experiment in section 6. The prediction capabilities
53 of the model is then discussed compared to a simpler von Mises model.

54 2. Experimental methods

55 2.1. Material

56 A 2024T351 aluminum alloy plate (hot rolled and 60 mm thick) was
57 obtained from Constellium. The nominal chemical composition is given
58 Tab. 1. According to the T351 specification, the sheet has been solution-
59 ized and quenched to produce a solute-rich solid solution. Ageing at room-
60 temperature generates a precipitation structure responsible of the strength-
61 ening. A final step consists in stress-relieving by application of a 1 percent
62 tensile strain uniformly in the rolling direction.

Al	Si	Fe	Cu	Mn	Mg	Cr	Ni	Zn	Ti	Zr
bal	0.06	0.13	4.1	0.51	1.4	0.01	41 ppm	0.1	0.02	0.02

Table 1: Chemical composition of the studied Al2024T351 plate (weight %).

63 The as-received material has been analyzed in terms of microstructure
64 and composition as a function of the plate thickness. In the next, L, T and S
65 classically denote the longitudinal rolling, transverse and normal directions

66 of the plate, respectively. Samples aligned with the L, S, T directions were
67 machined from the plate to characterize the microstructure on faces L-S and
68 T-S using techniques described in Fig. 1. Hereafter, Z (mm) represents the
69 coordinate along the S direction with the origin ($Z = 0$) being located on
70 the symmetric mid plane of the plate. Care was taken to ensure that the full
71 domain from $Z = 0$ to $Z = 30$ mm was analyzed in terms of microstructure
72 and its evolution along the half-thickness.

73 *2.2. Microstructure*

74 Material coupons were carefully polished using SIC grid followed by di-
75 amond past (struers) on a rotary wheel to obtain a mirror finish on both
76 L-S and T-S faces. First, Vickers hardness has been measured along a line
77 from the sheet surface to the center every 0.5 mm. Second, a series of opti-
78 cal micrographs at magnification x10 were recorded, after a Keller reactive
79 attack to highlight grain boundaries. The grain size in the S direction has
80 been estimated every 2 mm by the line intercept method.

81 A large series of electron back-scatter diffraction maps (EBSD) was recorded
82 along the Z axis. An FEI Versa microscope was used at 30 keV with a work-
83 ing distance of 10 mm and a step size of 1 μm . 43 EBSD scans of 0.7 mm
84 \times 0.7 mm wide regions were stitched together to produce a continuous map
85 of 1 \times 30 mm in the L-S plane. Grain orientation and texture evolution was
86 quantified using the OIM software from EDAX.

87 The composition of the aluminum matrix (mass percent) in copper (Cu),
88 iron (Fe), magnesium (Mg) and manganese (Mn) has been determined by
89 electron micro probe analysis (EMPA) every 100 μm along the Z axis.

90 *2.3. Mechanical testing*

91 *2.3.1. Flat tensile specimens*

92 To characterize the plastic properties of the material, a set of 63 flat
93 ($S_0 = 10 \text{ mm} \times 3 \text{ mm}$) tensile specimens (TR) have been extracted from
94 the plate. Each specimen position is determined by 2 parameters: Z for
95 the position along the half-thickness and θ for the orientation in the T-L
96 plane. A specimen aligned with the L direction corresponds to $\theta = 0^\circ$.
97 Nine depths: $Z \in [0.5, 4, 7.5, 11, 14.5, 18, 21.5, 25, 28.5]$ (mm) and five angles:
98 $\theta \in [0^\circ, 22.5^\circ, 45^\circ, 67.5^\circ, 90^\circ]$ have been examined. Several tests are doubled
99 or realized in the opposed half-thickness to check plate symmetry The local
100 frame attached to the specimen is denoted (1, 2, 3). Axis 1 is along the tensile

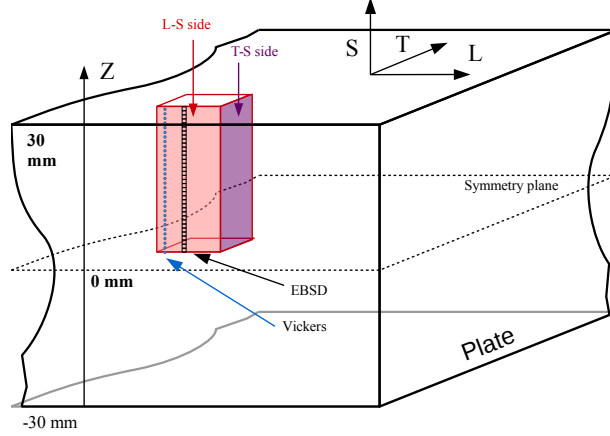


Figure 1: Material samples (30 mm \times 10 mm \times 10 mm) extracted from the thick plate for microstructure characterization.

101 direction, axis 2 is along the width and axis 3 the specimen thickness which
 102 is always identical to S.

103 Specimens were tested up to failure on a servo-hydraulic machine with
 104 two extensometers: one along direction 1 (specimen length) and the other
 105 along direction 2 (specimen width). Both extensometers provide nominal
 106 strains: $\varepsilon_{11} = \Delta L / L_0$ and $\varepsilon_{22} = \Delta w / w_0$ ($L_0 = 25$ mm, $w_0 = 10$ mm). ε_{ii} denotes
 107 the axial strain along direction i ($i = 1, 2$ or 3) and ΔL and Δw are the
 108 extensometers extension/closure. S_0 the initial cross section. The reaction
 109 force F is measured and provides the nominal stress $\sigma_{11} = F / S_0$, stress along
 110 loading direction. Plastic deformations ε_{11}^p and ε_{22}^p can then calculated by
 111 subtracting the elastic part of the strain using the mean value of the Young
 112 modulus $E = 73500$ MPa.

113 The material response under different loading conditions will be ana-
 114 lyzed in terms of yield stress at 0.2% plastic strain $R_{0.2}$, ultimate tensile
 115 stress R_m and Lankford coefficient r_θ . The Lankford coefficient is used to
 116 quantify plastic anisotropy and is calculated according to the expression
 117 $r_\theta = -\varepsilon_{22}^p / (\varepsilon_{11}^p + \varepsilon_{22}^p)$. It is commonly applied to evidence anisotropy: if
 118 $r_\theta = 1$, the material is perfectly isotropic otherwise it is anisotropic.

119 2.3.2. Axisymmetric notched tensile specimen

120 Axisymmetric notched tensile (NT) specimens (see Fig. 2b) have been
 121 extracted at $Z = 0$ mm in three directions ($0^\circ, 45^\circ, 90^\circ$). For each direction,

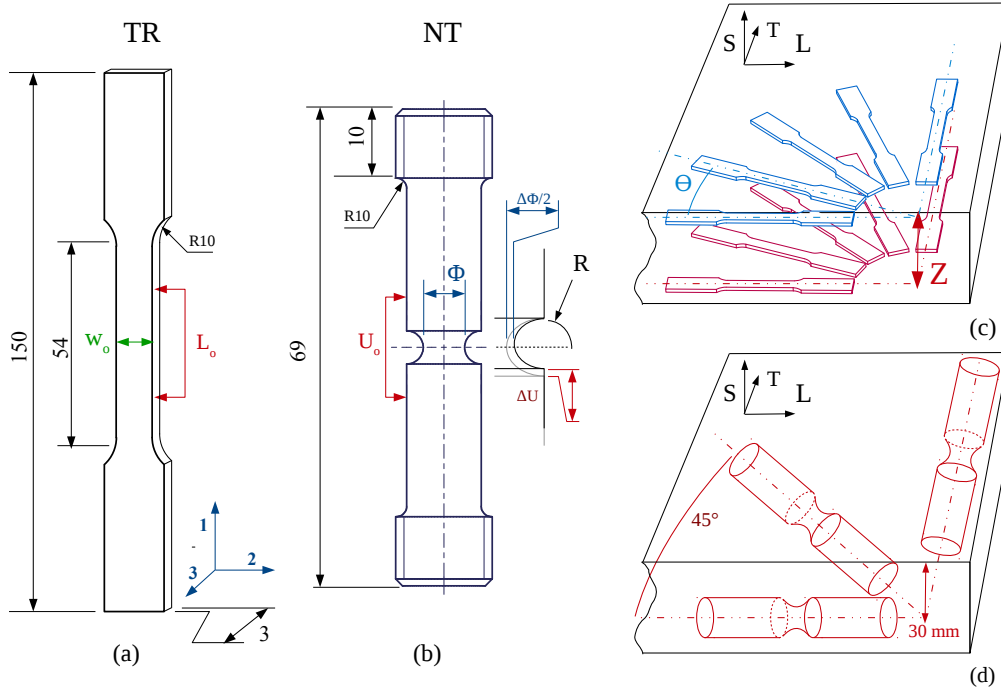


Figure 2: (a) Tensile geometry specimen with longitudinal (red) and lateral (green) extensometers, L_o and w_o are the initial dimensions; (b) Axisymmetric notched geometry specimen with length (red) and section (blue) extensometers, U_o and Φ_o are the initial dimensions; (c, d) Schematics showing the extraction of tensile and NT specimens at different angles θ and depth Z from the 2024T351 plate.

122 three different radii geometries were machined (NT2, NT4, NT10). The ini-
 123 tial radius r is related to the ξ value in the NT ξ convention by the equation:
 124 $\xi = 10r/\Phi_0$ (initial central section $\Phi_0 = 6$ mm and Φ actual central section).
 125 For the mechanical test to failure, specimens were mounted in the
 126 servo-hydraulic machine and displacement was imposed on the specimen's
 127 head. An extensometer in the horizontal plane measures continuously the
 128 central section diameter $\Delta\Phi$ (along the S direction) and a second one in the
 129 vertical plane, measures the notch opening ΔU ($U_0=10$ mm). Both exten-
 130 someter deformations $\Delta U/U_0$ and $\Delta\Phi/\Phi_0$ will be used for comparison in the
 131 simulations of the material behaviour (see section 5).

132 2.3.3. Panel structure

133 Beside material coupons, a large panel structure has been studied and
 134 subjected to cold forming process (cf. Fig. 3). The part is composed of a

135 3 mm skin associated with two crossed stiffeners in the center. A panel has
 136 been machined from the studied plate and cold-bent to produce a residual
 137 angle of 4.5° , typical of the bending angle used in aircraft fuselage panel
 138 forming. The top of the central stiffener is maintained by a support and a
 139 displacement ΔZ is imposed on both skin sides (cf. Fig. 3c). The panel is
 140 then unloaded.

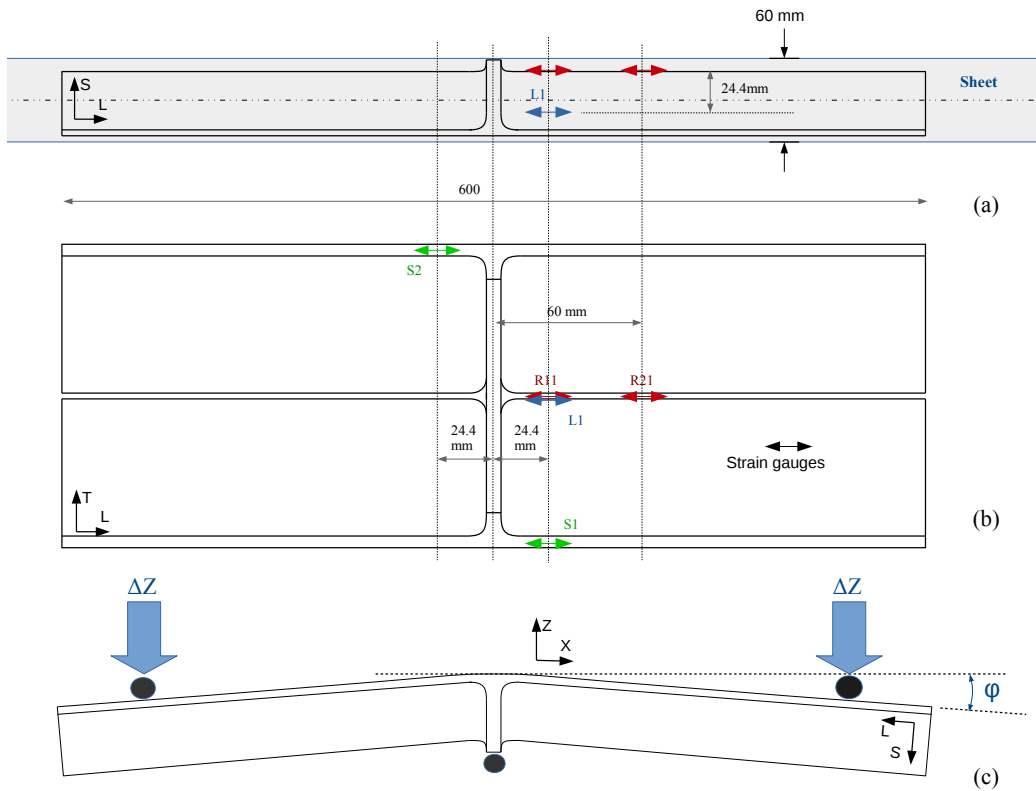


Figure 3: (a) Side view of the panel structure extracted from the plate, (b) top view of the panel geometry (not to scale for clarity) with gauges (symbol \leftrightarrow) placed on the specimen, (c) schematics of the 3 points bending test applied to the panel; the support are placed 550 mm apart, symmetrically with respect to the center of the panel.

141 The bending test is monitored by a set of six strain gauges fixed in dif-
 142 ferent locations perpendicularly to the bending axis. No load cell or pre-
 143 cise displacement sensor being installed on this large machine, the force and
 144 the displacement are not recorded during the test. The positions of the
 145 gauges have been chosen adequately to capture representative strain evo-

146 lutions through the structure (cf. Fig. 3b where all positions have been
147 marked). For instance, R11 has been placed at the top of the stiffener where
148 the highest values of plasticity is expected.

149 3. Microstructure characterization across the sheet thickness

150 3.1. Matrix composition and hardness

151 EMPA measurements (see Fig. 4) showed that alloy components mass
152 percent composition in the matrix does not vary significantly as a function
153 of Z and is close to the specification values (the observed scatter remains
154 within 8%). A depletion of 10% in Cu close to the plate center is however
155 observed. The hardness value is rather constant through the thickness at
156 $145 \text{ HV} \pm 5\%$ with a small gradient from the center (harder) to the surface
157 (softer) in both T-S and L-S planes (see Fig. 5a).

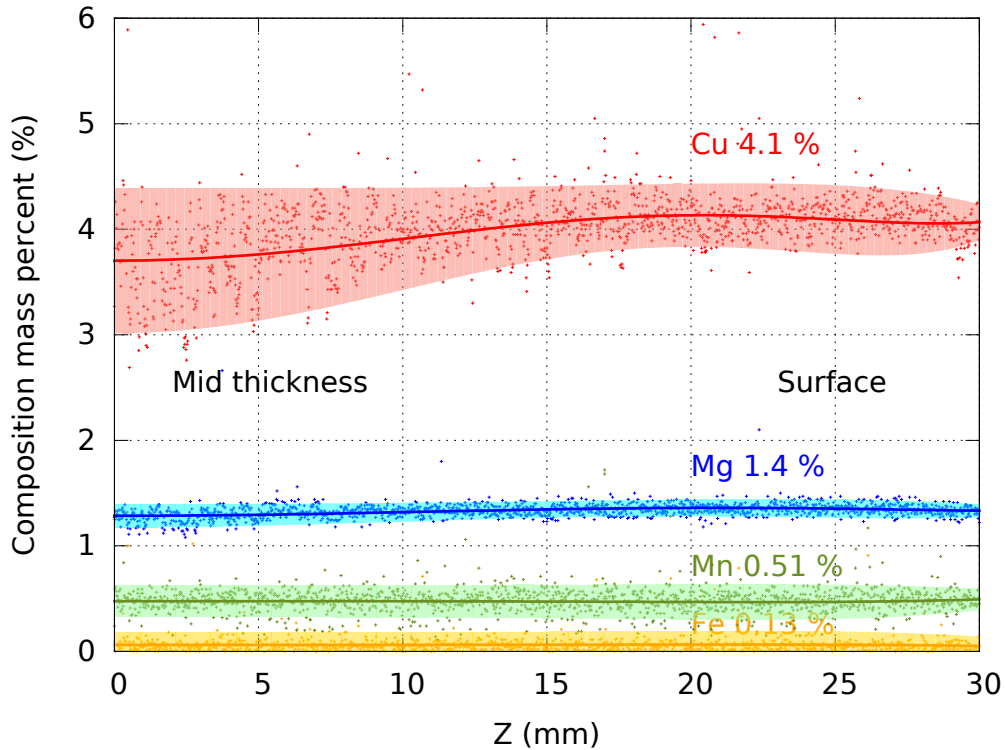


Figure 4: Mass percent composition of Iron, Copper, Magnesium and Manganese in aluminum matrix along half-thickness sheet (L-S plane).

158 *3.2. Grains and crystallographic texture*

159 Grains shapes and crystallographic texture show a strong evolution as
 160 a function of the depth in the plate. In agreement with many other rolled
 161 materials, grains are elongated in the rolling direction and flat in the thickness
 162 direction but grains are much smaller in the plate center. The equivalent
 163 grain size in the S direction shows a significant gradient (Fig. 5c). This is
 164 directly visible on the micrographs (Fig. 5b,d) and EBSD maps (see Fig. 7).

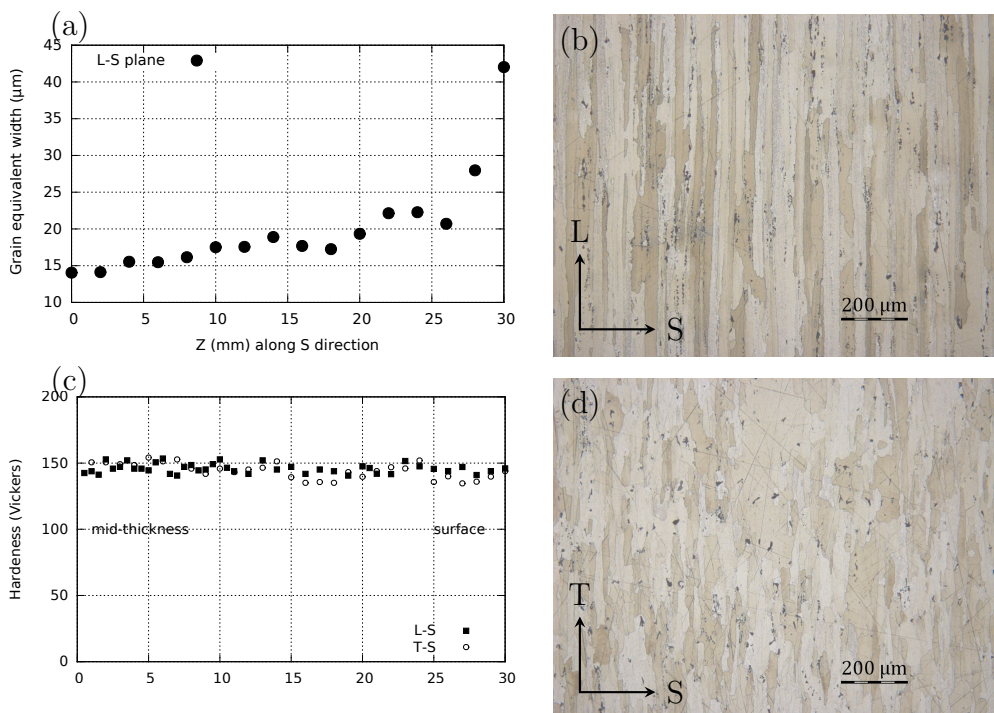


Figure 5: (a) Equivalent grain width and vickers hardness (c) along L-S and T-S plane and microstructure in sheet center layer for L-S (b) and T-S (d) plane for $Z = 14$ mm.

165 The grains are heavily deformed by the rolling process, causing crystal
 166 rotations and results in a modification of the crystallographic texture. This
 167 texture evolution during rolling for aluminum alloy has been extensively dis-
 168 cussed in the literature [11, 13–15, 17–19]. The rolling process is known
 169 to induce plane strain compression in the central layer of the plate and high
 170 shear strains in the sub-surface plate layers [14, 18, 20]. The different loading
 171 paths generate distinct textures: for aluminum alloys, rolling favors growing

172 of brass texture $[011] \langle 211 \rangle$ or $[011] \langle 111 \rangle$ in the plate center and *shear* texture
173 $[001] \langle 110 \rangle$ in the sub-surface layer [11, 14, 18, 19]. The ratio between center
174 and sub-surface textures increases with the reduction ratio [13, 14, 17, 18].

175 Fig. 6 shows pole figures at different depths in the plate and confirm
176 this trend. Four different regions can be distinguished where the texture
177 transition from *brass* in the plate center to a recrystallized texture at the
178 surface. From $Z = 0$ to 10 mm (mid-thickness), the material is strongly
179 *brass* and *cube* textured (see Fig. 6a). In the quarter thickness layers, *brass*
180 texture is less visible and a *shear* texture appear (see Fig. 6b). In the sub-
181 surface region ($Z > 20$ mm), a recrystallized texture has appeared and the
182 *shear* texture has essentially disappeared (see Fig. 6c). Finally at the surface
183 of the plate the material displays a very large number of crystal orientations
184 without any visible texture (see Fig. 6d).

185 The change in texture close to the plate surface is caused by the recrystal-
186 lization phenomenon. It is well established that material can completely or
187 partially recrystallize after rolling process [17, 19]. It's known that when the
188 stored energy is exceeding a threshold, it can contribute to grains bound-
189 aries motion and trigger the nucleation and growth of new grains. This
190 phenomenon is thermally activated, with a recrystallization temperature of
191 $0.4 \times T_f$ in metals, with T_f the fusion temperature. The plastic stored energy
192 takes part in the driving force and increase recrystallization rate. In addition,
193 the recrystallization temperature decreases with increasing deformation [21].

194 Past research on recrystallization in rolled aluminum alloys showed that
195 process conditions like deformation level, initial texture, particles distribu-
196 tions and temperature can affect recrystallized grain size and texture [21].
197 Recrystallization leads to texture mitigation and to a decrease of the fraction
198 of high-angle boundaries in the material. For thick aluminum plates, the roll
199 velocity ratio (both in hot and cold rolling) was pointed out to be impor-
200 tant [17]. After deformation and annealing, *shear* texture almost disappear
201 in the sub-surface layers leaving random crystallographic orientations and
202 modified grains morphology while material remains unchanged in the sheet
203 center [19, 21]. This is caused by heterogeneity in the strain fields during the
204 process and hence in the stored plastic energy after rolling.

205 EBSD maps in the L-S plane presented on Fig. 7 clearly highlight the
206 morphology and texture differences through thickness. Un-recrystallized
207 rolled material can be recognized by longer and fragmented grains featur-
208 ing a high density of sub-grains and a larger orientation spread through the
209 grain. Recrystallized grains have different attributes: the size is larger in the

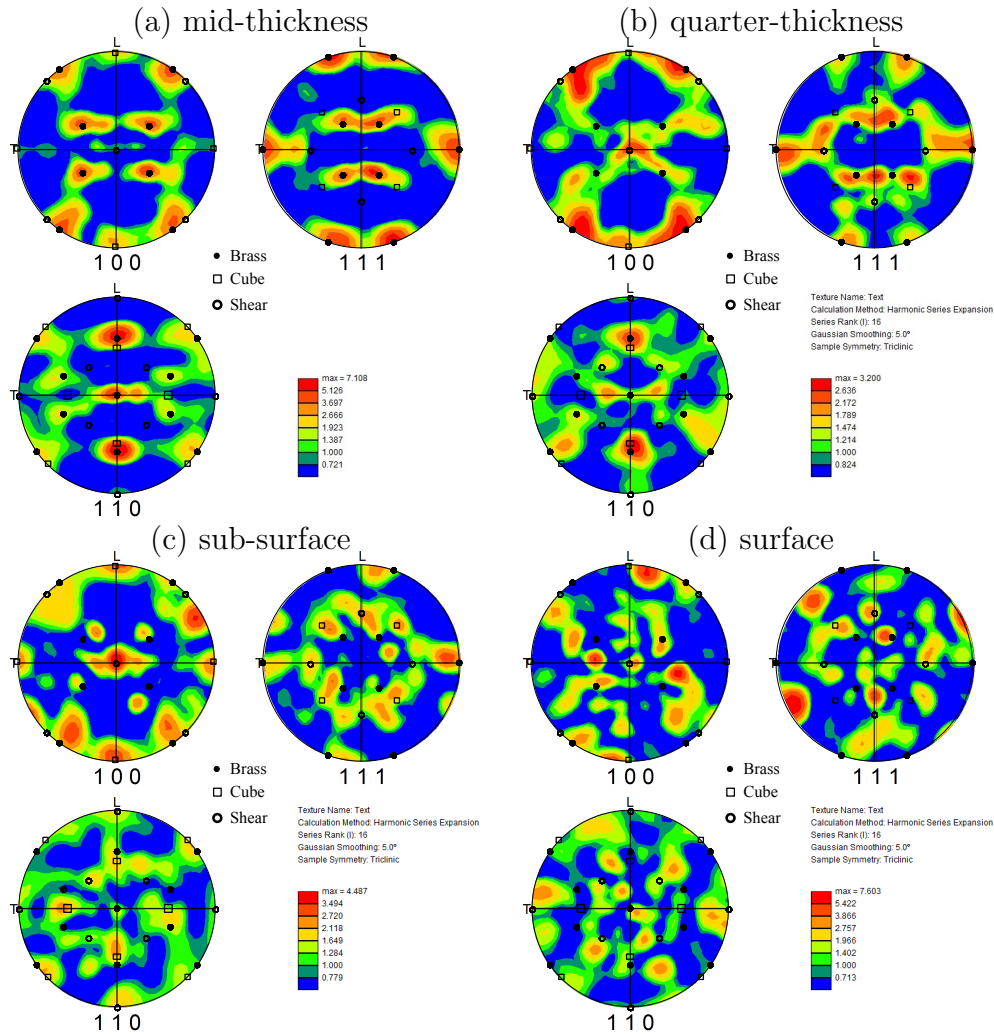


Figure 6: Pole figures computed from selected EBSD scans (a) mid-thickness region ($Z = 3.8$ mm), (b) quarter-thickness region ($Z = 13.6$ mm), (c) sub-surface region ($Z = 23.3$ mm) and (d) surface ($Z = 29.6$ mm); elementary textures *cube*, *brass* and *shear* have been superimposed for comparison

210 S direction and smaller in the L direction. In addition, they have very little
 211 sub-grains and display an homogeneous crystallographic orientation typically
 212 lower than 1° . The average misorientation calculated for each grain in the
 213 4 regions is depicted on Fig 7 right. Recrystallized grains clearly appear in

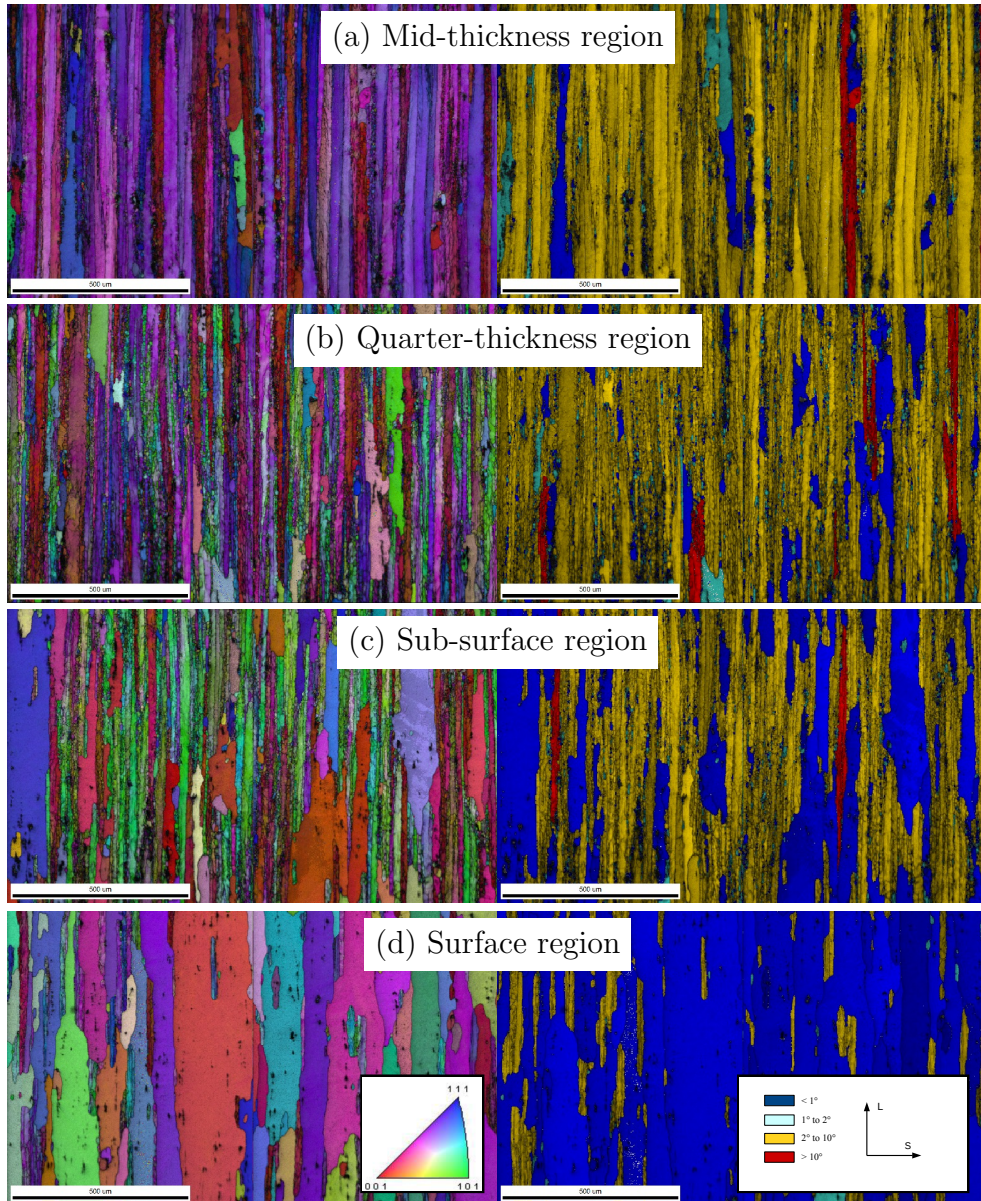


Figure 7: Selected maps from the EBSD scan series representative of the 4 regions: (a) $Z = 3.8$ mm, (b) $Z = 13.6$ mm, (c) $Z = 23.3$ mm and (d) $Z = 29.65$ mm; inverse pole figure maps and grains boundaries (15° of misorientation) are displayed on the left while crystal misorientation spread are displayed on the right.

214 blue, which is associated with a misorientation range below 1° . For higher
 215 misorientation, the material is considered un-recrystallized. Processing the
 216 complete EBSD scan series allows to plot the recrystallization ratio (as ob-
 217 tained by the surface ratio of recrystallized over un-recrystallized grains)
 218 as a function of Z (see Fig. 8). The four regions appear clearly: the material is
 219 completely un-recrystallized from $Z = 0$ to 8 mm (mid-thickness), transition
 220 to partially recrystallized from $Z = 8$ mm to 17 mm (quarter-thickness), par-
 221 tially recrystallized from $Z = 17$ mm to $Z = 27$ mm (sub-surface) and finally
 222 is completely recrystallized at the surface of the plate. Additional EBSD
 223 scans carried out along the other half-thickness showed symmetric results
 224 with respect to the plate median plane $Z = 0$.

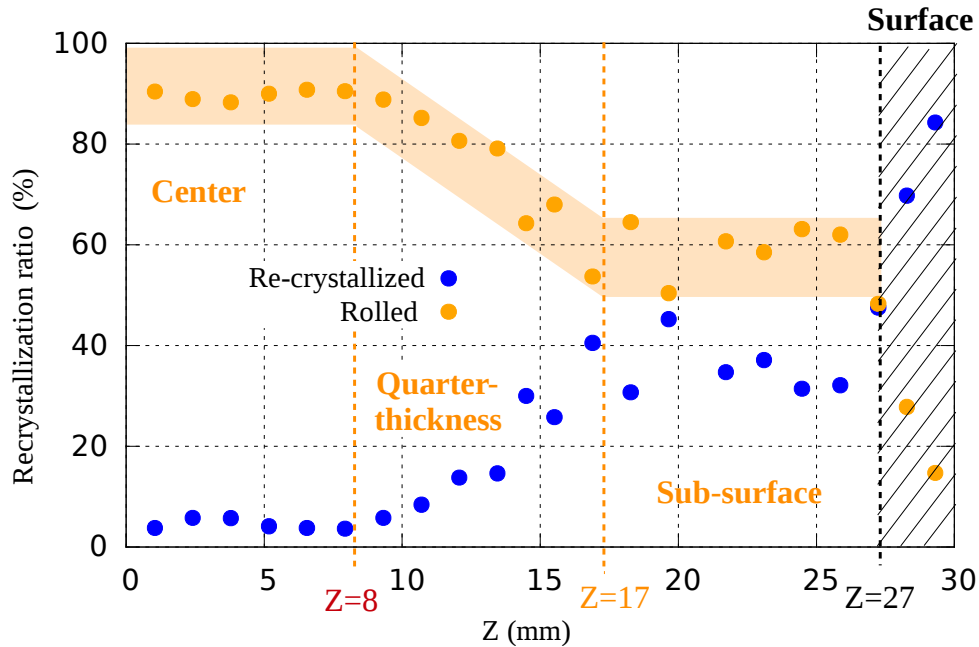


Figure 8: Evolution of the recrystallization ratio (as computed by the surface ratio) along the plate thickness (Z axis).

225 This reveals a strong evolution of the microstructure through the thick-
 226 ness in terms of texture, grain shape and dislocation content. This hetero-
 227 geneity is likely to impact significantly the mechanical properties and create
 228 a gradient in the thickness of the plate.

229 4. Elasto-plastic properties

230 Results of the tensile test series are presented in Fig. 9. First, stress *vs*
231 plastic strain curves for specimens extracted along L ($\theta = 0^\circ$) for different
232 depths (varying Z) show a consistent increase in the flow stress level from
233 the surface to the center of the plate. The difference in material strength
234 (both yield stress and ultimate tensile stress) is as high as 20%, the mid-
235 thickness shows enhanced properties compared to the sub-surface region.
236 It should be noted that the difference in terms of yield stress is stronger
237 than that was observed by micro-hardness. Engineering strain at fracture
238 decreases consistently when the strength increase: from 22% (sub-surface) to
239 15% (mid-thickness).

240 Note that in the configuration ($Z = 18$ mm, $\theta = 0^\circ$), Portevin-Le Chate-
241 lier instabilities appear. Serration are visible on stress-strain curve which can
242 be attributed microscopically to the dynamic interaction of mobile disloca-
243 tion and solute atoms [22]. It's known to be dependent of temperature and
244 strain rate [23].

245 The elastic modulus has been measured and no significant evolution has
246 been measured. The average value is 73500 MPa with a variance of 1100
247 MPa. The Poisson coefficient is 0.34.

248 Results are presented at the plate mid-thickness ($Z = 0.5$ mm, varying
249 θ) in Fig. 9b. Here, the effect of stretching as part of the T351 condition
250 is clearly visible (see Fig. 9b) with a sharper elastic-plastic transition and
251 an increased flow stress for the specimen machined in the rolling direction
252 ($\theta = 0^\circ$) compared to all other directions.

253 The evolution of R_m both with the depth of the specimen in the plate
254 and the angle with the rolling direction are depicted in Fig. 9e. Two main
255 points can be highlighted. First, the planar anisotropy is stronger in the
256 mid-thickness region of the plate which can be attributed to the strong *brass*
257 texture revealed by the EBSD analysis in this region (see section 3.2). Sec-
258 ond, a decrease of R_m from the mid-thickness to the surface is observed in the
259 L direction and in the T direction (to a smaller extend) but is not observed
260 for $\theta = 45^\circ$ or $\theta = 67.5^\circ$. This reveal a complex interplay between texture
261 and plastic anisotropy.

262 An average Lankford coefficient is evaluated from the linear part of ε_{22}^p vs
263 $-(\varepsilon_{11}^p + \varepsilon_{22}^p)$ curves (see Fig. 9c,d). r_θ is distributed around 0.5 in the plate
264 sub-surface, which reveals a strong out-of-plane anisotropy (see Fig. 9f). In
265 contrast, close to the center of the plate, r_θ transition from 0.5 towards the

266 rolling direction to 1 towards the transverse direction.

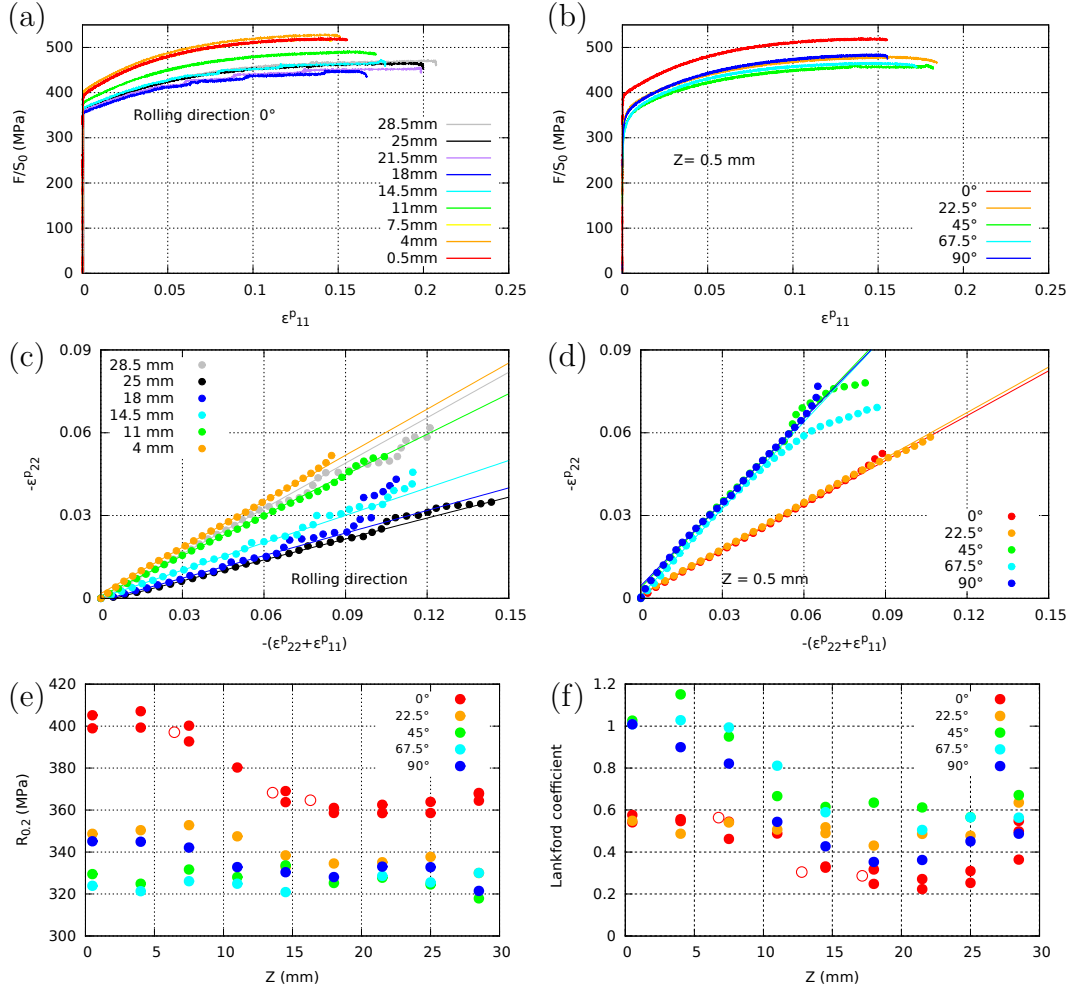


Figure 9: Experimental stress-strain and Lankford curves of the specimens in the rolling direction (a)(c) or at $Z = 0.5$ mm fixed (b)(d). Yield strength and Lankford coefficient in function of Z and θ (e)(f). Results for $Z < 0$ appear with open circles to show the material symmetry with respect to the mid plane.

267 Overall, a close inspection of the through-thickness evolution of the me-
 268 chanical properties can be split into 4 different layers in the half-thickness
 269 ($|Z| \in [0, 8]$ mm (Mid-thickness), $|Z| \in [8, 17]$ mm (Quarter-thickness),
 270 $|Z| \in [17, 27]$ mm (Sub-surface), $|Z| \in [27, 30]$ mm (Surface)) which closely
 271 follow the texture evolution (see Fig. 8).

272 At this point, the complex plastic properties of the thick Al2024T351
 273 plate have been quantified by both the anisotropy in the L-T plane and
 274 heterogeneity of the plastic properties in the S direction. A strong gradient
 275 of plastic properties in the thickness has been revealed which itself depends
 276 on the angle between the loading and rolling directions. In the next section,
 277 a constitutive behaviour that can reproduce the variability of the properties
 278 will be selected and the material parameters will be identified.

279 5. Constitutive modelling

280 5.1. Material model

281 To model the material behaviour, a phenomenological approach using
 282 an anisotropic Hill yield function and an isotropic hardening function $R(p)$
 283 has been adopted [24]. The Hill formulation is based on the following yield
 284 function:

$$f(\bar{\sigma}, R) = \bar{\sigma} - R(p) \quad (1)$$

285 There, the equivalent stress $\bar{\sigma}$ is a modified von Mises expression inserting a
 286 fourth order tensor \mathcal{H} to describe material anisotropy [25]:

$$\bar{\sigma} = \sqrt{\frac{3}{2} \mathbf{s} : \mathcal{H} : \mathbf{s}} \quad (2)$$

287 where \mathbf{s} is the stress deviator. The anisotropy tensor (\mathcal{H}) reduces to 6 com-
 288 ponents denoted h_{LL} , h_{TT} , h_{SS} , h_{LT} , h_{TS} and h_{SL} :

$$\bar{\sigma} = \sqrt{\frac{3}{2} (h_{LL}s_{LL}^2 + h_{TT}s_{TT}^2 + h_{SS}s_{SS}^2 + 2h_{LT}s_{LT}^2 + 2h_{TS}s_{TS}^2 + 2h_{SL}s_{SL}^2)} \quad (3)$$

289 Following [3], to model the material work hardening, an isotropic non-linear
 290 law with a linear term and two exponential terms has been selected. The
 291 isotropic hardening function $R(p)$ is expressed as:

$$R(p) = R_0 [1 + K_0 p + K_1(1 - e^{-b_1 p}) + K_2(1 - e^{-b_2 p})] \quad (4)$$

292 where the variable p is the accumulated plastic strain such that: $\bar{\sigma} \dot{p} = \boldsymbol{\sigma} : \dot{\boldsymbol{\xi}}_p$.
 293 The plastic strain rate given by $\dot{\boldsymbol{\xi}}^p = \lambda \partial \bar{\sigma} / \partial \boldsymbol{\sigma}$ and $\lambda = \dot{p}$ is the plastic
 294 multiplier. This allows a fine description of the stress-strain curves as b_1 and

295 b_2 give enough degrees of freedom to simulate saturating rate for both low
296 and high deformation [26]. In total, the model has 12 material parameters,
297 6 for the plastic anisotropy and 6 for the work hardening behaviour.

298 With the chosen model, the sharper elasto-plastic transition due to pre-
299 stretching in the L direction cannot be accurately captured. This could
300 be achieved using an additional kinematic hardening combined with the Hill
301 yield criterion. Combined isotropic-kinematic hardening are useful to predict
302 complex load path changes [27]. However as pre-stretching is typically limited
303 to 1%, the effect would be limited to early plastic deformation and has not
304 been considered here.

305 5.2. Material parameters identification

306 The material parameters are identified by fitting the model response to
307 all the experimental tension curves available. In order to represent plastic
308 properties gradient along the S direction, the material parameters are identi-
309 fied for each of the 4 Z layers of the experimental recognized in the data base
310 (see section 4): *Center*, *Quarter-thickness*, *Sub-surface*, *Surface*. The value
311 of R_0 is imposed as identical for all layers. No shear test required to identified
312 h_{TS} and h_{SS} being available, both values are fixed equal to 1. Note that in a
313 three-point bending test, the different layers will experience different shear
314 stresses and strains. Conducting shear tests would therefore be of interest.

315 The 9 parameters K_0 , K_1 , K_2 , b_1 , b_2 , h_{LL} , h_{TT} , h_{SS} , h_{LT} (R_0 being fixed)
316 have been identified via an optimization procedure to best fit the experi-
317 mental curves simultaneously: σ_{11} vs ε_{11}^p (A) and ε_{11}^p vs ε_{22}^p (B) with five
318 directions θ and all Z in yield selected: $|Z| \in [0, 8]$ mm for *Center* paramet-
319 ers, $|Z| \in [8, 17]$ mm for *Quarter-thickness*, $|Z| \in [17, 27]$ mm for *Sub-surface*
320 and $|Z| \in [27, 30]$ mm for *Surface* (see Tab. 2). One should note that the
321 value of R_0 does not directly represent the yield stress which is here defined
322 non uniquely by a combination of R_0 and the h coefficients. Fixing R_0 allows
323 avoiding a redundant parameter in the optimisation procedure. All simu-
324 lations have been conducted using the FE software Z-set [28] and selected
325 results have been reported on Fig. 10. It can be noticed that the model de-
326 scribes well the experimental tests (data represented by points) that either
327 for the stress evolution (see (a) and (b)) but also regarding the anisotropy
328 by the strain evolution (see (c) and (d)). Results for all thicknesses Z and
329 material directions θ , which represent 45 different curves, match equally well.
330 Some discrepancies can nevertheless be seen on the transverse plastic strains.

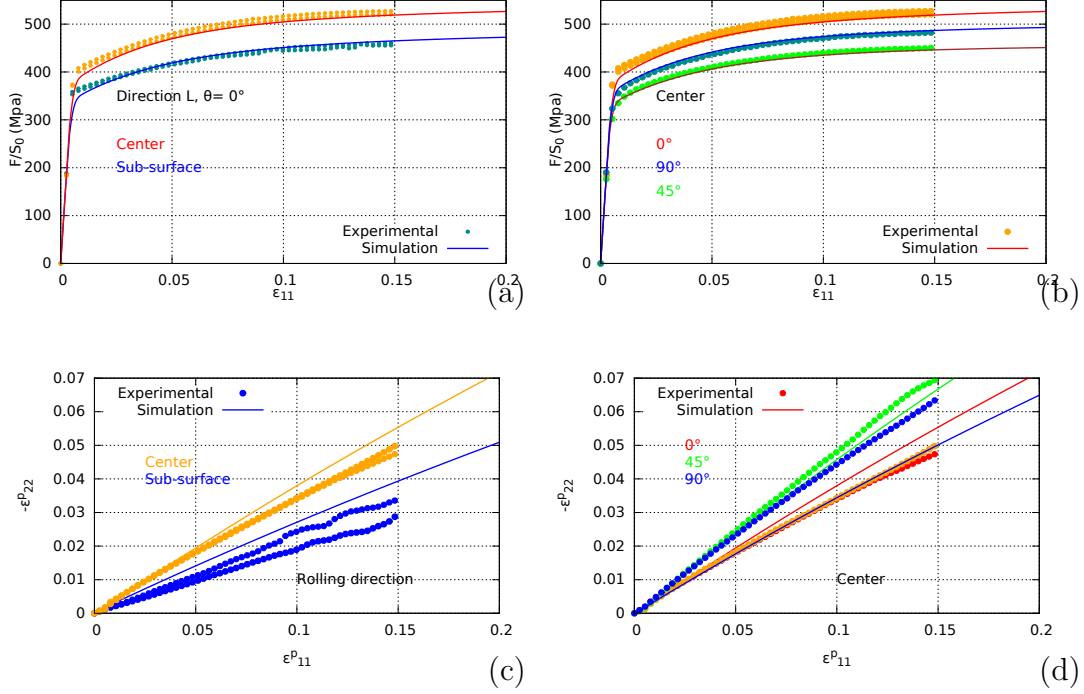


Figure 10: Stress-strain curves for experimental test and material model in the rolling direction (fixed direction) (a) or in the *Center* layer (fixed Z) (b). Transverse ϵ_{22}^p plastic deformation in function of longitudinal ϵ_{11}^p plastic deformation for experimental test and simulation in the rolling direction (c) or in the *Center* layer (d).

331 It turns out that the agreement is good at $\theta = 45^\circ$, but that the Lankford
 332 coefficient is slightly underestimated at 0° and overestimated at 90° .

Z (mm)	R_0	K_0	K_1	b_1	K_2	b_2	h_{LL}	h_{TT}	h_{SS}	h_{LT}
Center	210	1.87	0.303	950.	0.403	20.	0.458	0.585	0.7	0.676
Quarter-thickness	210	1.903	0.316	950.	0.385	20.	0.508	0.589	0.896	0.609
Sub-surface	210	2.209	0.332	950.	0.36	20.	0.602	0.503	1.120	0.559
Surface	210	2.21	0.332	950.	0.36	20.	0.570	0.509	1.11	0.554

Table 2: Material model parameters identified for each layer (R_0 , K_0 , K_1 and K_2 are given in MPa, h_{TS} and h_{SL} are kept equal to 1).

333 5.3. NT Tensile test simulation

334 The mechanical response of tensile tests on NT specimens has been sim-
 335 ulated using the identified behaviour. The response is compared to exper-

336 imental tests on specimens extracted at mid-thickness, where the material
337 anisotropy is the strongest. The purpose is to check the ability of the model
338 to properly represent deformation in condition of strong triaxiality, *without*
339 *including explicitly these tests in the identification database*. Three loading
340 directions and three triaxiality ratios have been investigated using respec-
341 tively the specimen orientations in the L-T plane and three different notch
342 radii (see Fig. 2).

343 Fig. 11 shows experimental and simulated F/S_0 vs $\Delta U/U_0$ and F/S_0 vs
344 $\Delta\Phi/\Phi_0$ curves for all investigated Z and θ values. The agreement between
345 the model and the experimental data is excellent for all three directions
346 and even for small radius (high triaxiality). It can be noticed that stress are
347 over-estimated just before failure because model include no damage criterion.
348 This confirm that the model is effective to simulate the strongly anisotropic
349 material behaviour, including when high triaxiality is involved.

350 No significant effect of the specimen orientation is observed experimen-
351 tally on the stress-strain response as in the case of the tension specimens.
352 This can be attributed to the high triaxiality. In that case the multiax-
353 ial stress state reduces anisotropy. It is observed that the *quasi-isotropy*
354 observed is well represented by the model which at the same time well repro-
355 duces the plastic anisotropy in pure tension (see Fig. 10b). In addition, one
356 can note that the final fracture occurs earlier in the case of $\theta = 90^\circ$. This
357 ductile behaviour has been studied previously and it can be attributed to the
358 second phase particles alignment along the rolling direction [29].

359 6. Bending simulation of a structure panel

360 6.1. Simulation setup

361 The panel structure geometry (see Fig. 3) has been meshed using quadratic
362 tetrahedrons. The mesh density has been increased close to the top of the
363 central stiffener. Bending boundaries conditions are visible in Fig. 12: a
364 single maximal displacement $\Delta Z = 31.7$ mm is prescribed on the central
365 stiffener and two lines of nodes at each end of the panel are blocked along
366 Z . These boundary conditions represent accurately the scale 1 experiment.
367 Directions 1, 2 and 3 are associated respectively to directions X, Y and Z .

368 In order to estimate the effect of plate heterogeneity/anisotropy on the
369 cold forming operation, four simulations have been performed with the same
370 boundary conditions (see Fig. 3 left) and four material configurations. The

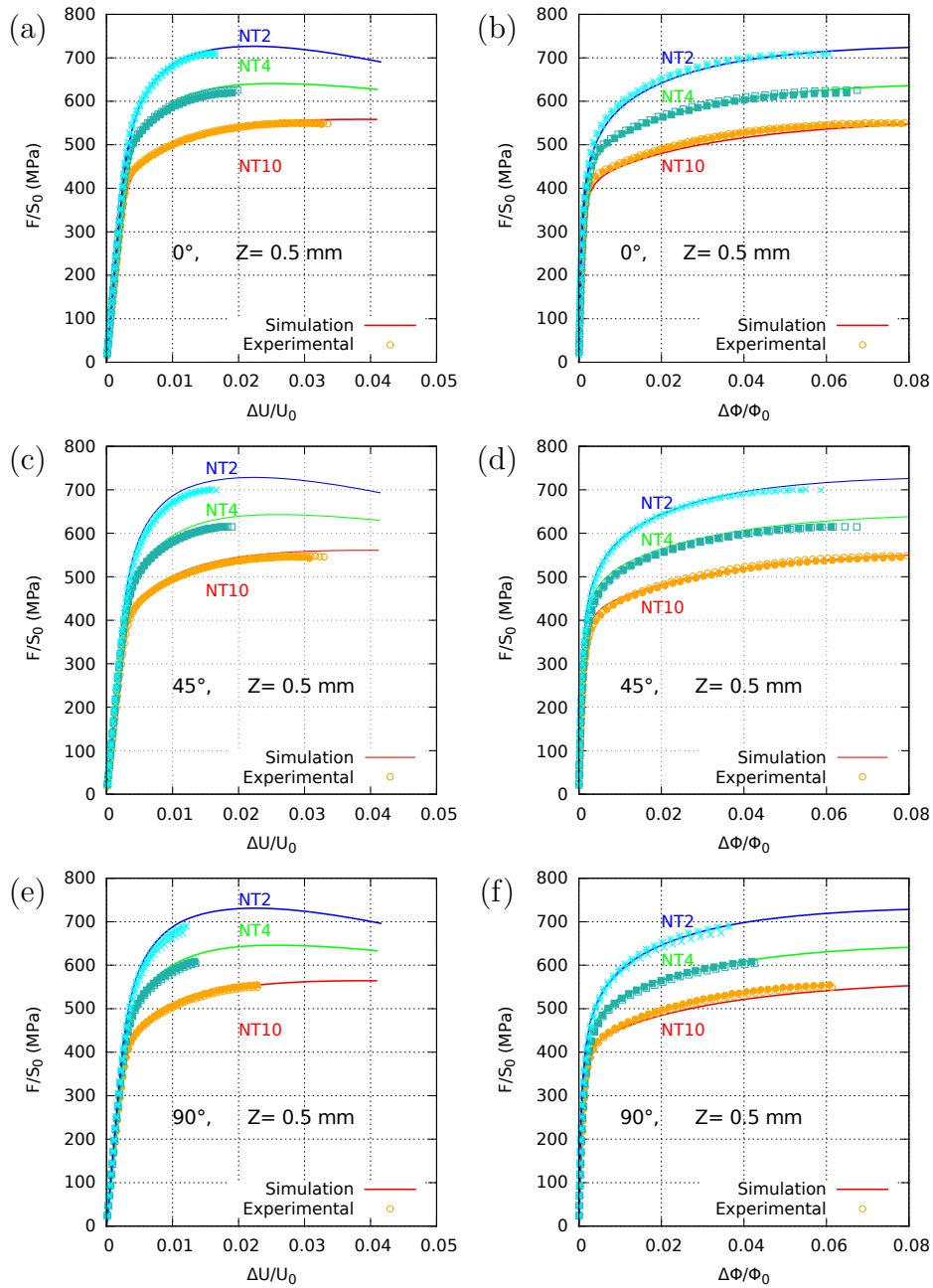


Figure 11: Experimental results and Simulations of the tension tests on notched specimens (NT2, NT4, NT10) loaded in 3 different directions $\theta = 0^\circ, 45^\circ, 90^\circ$. ΔU , $\Delta\Phi$ are longitudinal and diametral opening displacement.

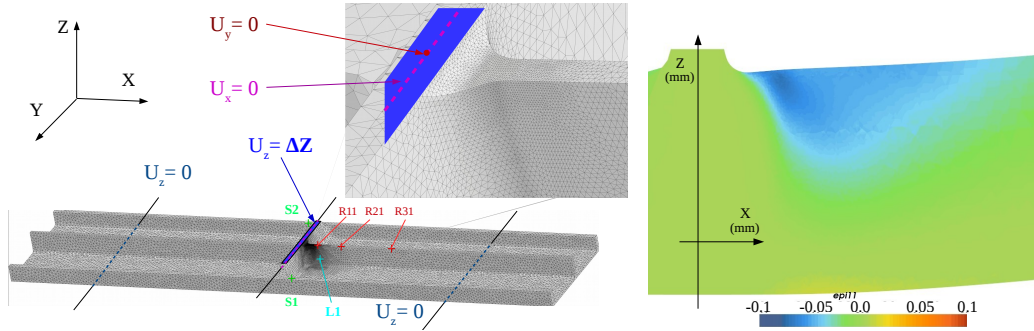


Figure 12: Panel specimen meshing and boundaries conditions of bending simulation (left), residual ϵ_{11}^p field close to the stiffener after simulating the bending process (right).

371 four models are defined by two different plastic criterion and two different spa-
 372 tial distributions of the material properties to represent the through-thickness
 373 gradient:

- 374 1. homogeneous von Mises criterion identified for the *Center* layer
- 375 2. homogeneous Hill criterion identified for the *Center* layer
- 376 3. homogeneous Hill criterion identified for the *Sub-surface* layer
- 377 4. heterogeneous Hill criterion identified at 4 different depths.

378 For model number 4, the analysis of the depth-resolved mechanical properties
 379 revealed that 4 main layers could be distinguished in the half-thickness (see
 380 Fig. 9 and Tab. 2), corresponding to 7 different layers accounting for the
 381 plate symmetry with respect to $Z = 0$. The mesh representing the structure
 382 panel has been divided into different element sets based on the center of mass
 383 of each element and the material properties assigned accordingly with the pa-
 384 rameters identified at *Center, Quarter-thickness, Sub-surface, Surface* respec-
 385 tively.

386 6.2. Results

387 The four simulations have been compared with the experimental bending
 388 test results on the structure panel. The value of strain ϵ_{11} at the experimental
 389 strain gauges locations is used *as numerical gauges* to monitor the quality
 390 of the simulation (see Fig. 12 for a visualization of the residual plasticity in
 391 the vicinity of the stiffener). The residual state, after forming and unloading
 392 showed that:

- 393 • the plasticity is essentially localized in the panel specimen in a state of
394 axial compression in direction L up to a maximum of -8%;
- 395 • significant residual stresses (mainly uniaxial and oriented along the L
396 direction) are present throughout the structure, the top of the stiffener
397 is under tension, the rest under compression.

398 Fig. 13a shows the comparison of the evolution of each gauge signal during
399 the bending simulation carried out with model 4 and during the experiment.
400 One can see that the model is in good agreement with all the gauges dur-
401 ing the test. The final level after bending as well as the strain level after
402 unloading (residual state) match within 5%.

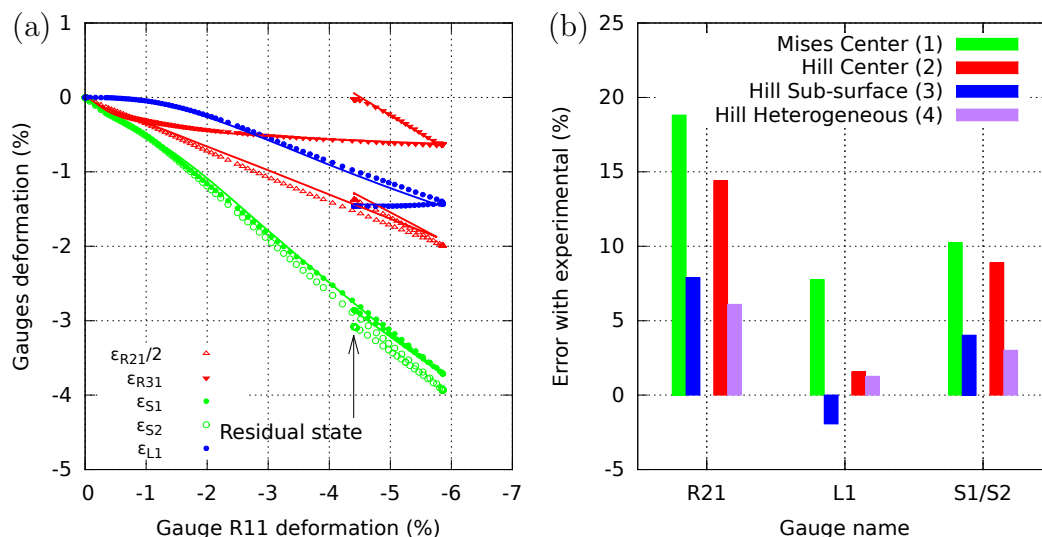


Figure 13: (a) Evolution of the simulated and experimental ϵ_{11} during the bending process using the heterogeneous Hill material model (the residual state denote the strain level after bending and after unloading); only half of the ϵ_{R21} gauge signal is plotted to improve readability (b) error difference between the simulated residual strain ϵ_{11} and experimental residual gauges deformations after bending and unloading (S1 and S2 gauge signals have been averaged).

403 The error at the final level after bending and unloading has been quan-
404 tified with the 4 different models tested and have been reported in Fig. 13b.
405 Note that R13 results were not included since the residual strain is very
406 close to zero. The homogeneous von Mises model clearly shows the poorest

407 performance with errors ranging from 8 to 18%, whereas the heterogeneous
408 Hill model shows the best predictions compared to experimental values with
409 errors ranging from 1 to 6%.

410 Comparing the model responses between them, the smaller gap between
411 Mises-Center and Hill-Center (1 and 2) than between the two homogeneous
412 Hill models (2 and 3) highlights a predominant effect of heterogeneity over
413 anisotropy. With Hill-Center, the agreement is better at gauges localized in
414 mid-thickness locations like $L1$, $S1$ and $S2$. Inversely, matching is better at
415 gauges localized in near-surface locations like $R11$, $R12$ and $R13$ with the
416 Hill-Sub-surface model. In view of its prediction capabilities, the heteroge-
417 neous Hill material model appears as the best compromise to conduct cold
418 forming simulation with thick plates. For simplicity, simulation were here
419 conducted using per-layer values of the material parameters. This could be
420 extended to identify each parameter as a function of the Z coordinate to
421 have smoother through-thickness evolution of the parameter values.

422 7. Conclusion

423 A microstructural and mechanical analysis of an 2024T351 Aluminium
424 alloy thick sheet were carried out at several depths. Our observations high-
425 light a strong microstructure gradient (texture and grain size) in the half
426 thickness, attributed to a partial recrystallization of the sheet after rolling.

427 A correlation has been established between this analysis and the plas-
428 tic property gradient also present along the half-thickness: a large series of
429 mechanical tensile tests is carried out using samples machined varying the
430 position along the thickness and the the orientation in the rolling plane. A
431 strong evolution of the plastic anisotropy between the center of sheet metal
432 and surface was shown. These through-thickness gradients have been mod-
433 eled in four homogeneous layers of mechanical properties and distinct mi-
434 crostructures.

435 An anisotropic constitutive model with non-linear work hardening has
436 been selected and identified using all available tensile tests. To reproduce
437 the gradient of mechanical properties in the depth of the plate, one set of
438 material parameters has been identified for each investigated depth. The
439 material identification has been further validated by comparison with the
440 response of notch-tensile test featuring different triaxiality ratios.

441 Finally a large structure panel bending test, representative of cold forming
442 industrial operations, has been carried out and simulated using the identi-

443 fied model. Simulation results are in very good agreement with experimen-
444 tal strain gauge signals located in different places of the structure. It was
445 shown that the identified model performs better than a simpler models non
446 accounting for anisotropy or through-thickness heterogeneity such as an ho-
447 mogeneous von Mises model.

448 8. References

- 449 [1] H. J. Bunge, K. Pöhlandt, A. E. Tekkaya, Formability of Metallic Mate-
450 rials: Plastic Anisotropy, Formability Testing, Forming Limits, Springer,
451 Berlin, Heidelberg, 2000. doi:10.1007/978-3-662-04013-3.
- 452 [2] D. Banabic, Sheet Metal Forming Processes, Springer-Verlag Berlin Hei-
453 delberg, 2010. doi:10.1007/978-3-540-88113-1.
- 454 [3] F. Bron, J. Besson, A yield function for anisotropic materials Applica-
455 tion to aluminum alloys, *Int. J. of Plasticity* 20 (2004) 937–963.
- 456 [4] J. C. Brem, F. Barlat, D. J. Lege, A generalized isotropic yield criterion,
457 *Int. J. of Plasticity* 3 (1991) 607–609.
- 458 [5] A. Karafillis, M. Boyce, A general anisotropic yield criterion using
459 bounds and a transformation weighting tensor, *J. Mech. Phys. Solids*
460 41 (1993) 1859–1886.
- 461 [6] I. The Aluminum Association, Rolling Aluminum: From the Mine
462 Through the Mill, The Aluminum Association, 1990.
- 463 [7] R. von Mises, Mechanik des plastischen Formänderung von Kristallen,
464 *Zeitschrift für Angewandte Mathematik und Mechanik* 8 (1928) 161–
465 185.
- 466 [8] A. Hershey, The plasticity of an isotropic aggregate of anisotropic face
467 centred cubic crystals, *J. of Applied Mechanics* 21 (1954) 241–249.
- 468 [9] W. Hosford, A generalize isotropic yield criterion, *J. Appl. Mech.* 39
469 (1972) 607–609.
- 470 [10] R. Hill, A theory of the yielding and plastic flow of anisotropic metals,
471 *Proceedings of the Royal Society of London. Series A, Mathematical and*
472 *Physical Sciences* 193 (1948) 281–297.

- 473 [11] I. Dillamore, W. Roberts, Preferred orientation in wrought and annealed
474 metals, ASM International, 2001.
- 475 [12] B. Bacroix, The influence of temperature on the rolling textures of al
476 alloys in the absence of recrystallization, *Materials characterization* 62
477 (2010) 22–34.
- 478 [13] J. Hirsch, Textures in aluminum forgings, *Textures and Microstructures*
479 14 (1991) 133–138.
- 480 [14] H. Weilan, Microstructure and local texture in hot rolled aluminum,
481 *Textures and Microstructures* 14 (1991) 647–652.
- 482 [15] J. Chen, Through-thickness texture gradient in aa 7055 aluminum alloy,
483 *Materials letters* 62 (2008) 88–90.
- 484 [16] R. Roumina, C. Sinclair, Deformation geometry and through-thickness
485 strain gradients in asymmetric rolling, *Metall and Mat Trans A* 39 (2008)
486 2495. doi:10.1007/s11661-008-9582-6.
- 487 [17] S. Wronski, Analysis of textures heterogeneity in cold and warm asym-
488 metrically rolled aluminium, *Materials characterization* 62 (2011) 22–34.
- 489 [18] L. Zhang, Texture, microstrucutre and mechanical properties of 6111
490 aluminum alloy subject to rolling deformation, *Materials Research* 14
491 (2017) 133–138.
- 492 [19] K. Lee, Effect of the hot-rolling microstructure on texture and surface
493 roughening of al-mg-si series aluminum alloy sheets, *Met. Mater. Int.* 17
494 (1991) 689–695.
- 495 [20] H. Jeong, Evolution of shear texture according to shear strain ratio in
496 rolled fcc metal sheets, *Metal and Materials* 12 (2006) 21–26.
- 497 [21] F. Humphreys, M. Hatherly, *Recrystallization and Related Annealing*
498 *Phenomena*, Elsevier, 2004.
- 499 [22] A. Van den Beukel, Theory of the effect of dynamic strain aging in
500 mechanical properties, *Physica StatusSolidi* 30 (1975) 197–206.
- 501 [23] A. Yilmaz, The portevin-le chatelier effect: a review of experimental
502 findings, *Sci Technol Adv Mater* 12 (2011) 1653–1662.

- 503 [24] R. Hill, *The Mathematical Theory of Plasticity* (1st ed, 1950), Oxford
504 Classic Texts in the Physical Sciences, 1998.
- 505 [25] F. Rivalin, J. Besson, A. Pineau, M. Di Fant, Ductile tearing of pipeline-
506 steel wide plates — II.: Modeling of in-plane crack propagation, *Engng*
507 *Fracture Mechanics* 68 (3) (2000) 347–364.
- 508 [26] J. Besson, G. Cailletaud, J.-L. Chaboche, S. Forest, *Nonlinear Mechan-*
509 *ics of Materials*, Springer, 2009.
- 510 [27] V. Tarigopula, O. Hopperstad, M. Langseth, A. Clausen, An eval-
511 uation of a combined isotropic-kinematic hardening model for rep-
512 resentation of complex strain-path changes in dual-phase steel, *Eu-*
513 *ropean Journal of Mechanics - A/Solids* 28 (4) (2009) 792–805.
514 doi:10.1016/j.euromechsol.2008.12.004.
- 515 [28] Zset-software, Mines ParisTech & ONERA, [http://www.zset-
software.com](http://www.zset-
516 software.com) (version 8.5).
- 517 [29] A. Benzerga, J. Besson, A. Pineau, Anisotropic ductile fracture: Part I:
518 experiments, *Acta Materialia* 52 (2004) 4623–4638.